

Energy Efficient and Fast Charging Nitrogen Doped Carbon Anodes Derived from BIAN-melamine Based Porous Organic Polymer for Lithium-ion Batteries

Bharat Srimita Mantripragada,^[a] Ms. Kottisa Sumala Patnaik,^[a] Koichi Higashimine,^[b] Rajashekhar Badam,^[a] and Noriyoshi Matsumi^{*[a]}

Fast charging anodes for lithium-ion batteries are most sought-after materials currently, owing to the increasing energy requirements of the world. In this context, carbonaceous materials are found to deliver faster kinetic performance in lithium-ion batteries. In this study, a single source of carbon and nitrogen was used as a precursor material to synthesize N-doped carbon (PyPBM600 and PyPBM800). The effect of synthetic conditions on the morphology of the material and in

turn on the electrochemical properties is presented. Anodic half-cells with PyPBM600 and PyPBM800 anodes showed excellent rate capability and capacity till 4 A/g for over 1000 cycles. Furthermore, full cell fabricated with PyPBM800 delivered extremely fast charging characteristics with 15-minute charging time, a reversible capacity of 1.2 mAh with a columbic efficiency of 99.8% and an enticing voltage and energy efficiencies of 90% for 300 cycles.

Introduction

The ability of fast charging in lithium-ion batteries is currently, the most sought-after characteristic. Though graphite anode is widely commercialised, problems such as anode polarisation, lithium metal plating impose restrictions on faster ion transport and charge transfer kinetics.^[1,2] These drawbacks are more pronounced at faster currents where the rate of mass transfer is faster than charge transfer. Lithium-ion transport within the anode plays a crucial role in achieving faster kinetics. It is known that the diffusion length (L) ($= \sqrt{\tau D_{Li^+}}$ (equation 0)), where τ is time of charging, D_{Li^+} is diffusion coefficient) is proportional to the time of charging i.e., as the length of diffusion increases, the time of charging increases and vice versa.^[3] In this background, a careful design on active material is necessary. From equation 1, the length of diffusion must be lowered to decrease the charging time. Hence, much effort is directed towards developing different morphologies of carbon like CNT,^[4] graphene^[5] etc., To overcome the problems faced with graphite anode, a possible strategy is to obtain turbostratic counterparts of graphite namely hard carbon. Due to the turbostratic nature of hard carbons, there is a possibility of faster lithium-ion diffusion and exposure of higher number of active sites.^[6] Komaba et al., demonstrated the application of sucrose derived hard carbon in Li, Na and K ion batteries. The

sucrose derived hard carbon was found to deliver excellent rate capability and in lithium-ion batteries, a highest reversible capacity of 550 mAh/g was observed.^[7] Besides these benefits, it is found that introducing heteroatoms like nitrogen was also found to contribute towards faster charging. Nitrogen being strongly electronegative ($\chi=3.4$) supports in faster kinetics by decreasing the charge transfer and diffusion barriers due to the stronger interactions between nitrogen and lithium cations.^[8] Inclusion of nitrogen also leads to the increase of pseudo capacitive charge storage process thereby further improving the kinetics of the battery.^[9] Qian-wang et al., demonstrated using density functional theory model that compared to pristine graphene nitrogen doped graphene shows lower diffusion barrier for lithium ions.^[10] Further, Jong-Sung et al., reported the application of N-doped carbon nano particles. A high reversible capacity of 596 mAh/g was obtained in lithium-ion batteries.^[11] To obtain nitrogen containing carbonaceous materials, various strategies like treating carbon materials with nitrogen rich chemicals like dopamine,^[12] melamine^[3] etc., are employed. However, in these strategies, efficient incorporation of nitrogen is not obtained, and the reaction is uncontrolled in nature. Among different strategies, synthesis of N-doped carbon using a single source of carbon and nitrogen is a unique strategy. Matsumi et al., reported an application of poly(benzimidazole) as a precursor for N-doped carbon and as a single source of carbon and nitrogen.^[3] One of the crucial advantages in this strategy is that the carbon and nitrogen are covalently linked in the conjugated network of the polymer. This increases the probability of nitrogen incorporation in the carbon framework. In this context, though various reports are available on the utilization of conjugated polymers as precursors for N-doped carbon, there is a lack of understanding on the suitable temperature for synthesis. Synthetic conditions such as temperature show a great impact on the morphology of the material.^[13] These morphological characteristics in turn impact

[a] Dr. B. S. Mantripragada, Ms. K. S. Patnaik, Dr. R. Badam, Prof. N. Matsumi Graduate School of Advanced Science and Technology, Japan Advanced Institute of Science and Technology (JAIST), Nomi, Ishikawa 923-1292, Japan
E-mail: matsumi@jaist.ac.jp

[b] Mr. K. Higashimine
Centre for Nano Materials and Technology, Japan Advanced Institute of Science and Technology (JAIST), Nomi, Ishikawa 923-1292, Japan

 Supporting information for this article is available on the WWW under <https://doi.org/10.1002/batt.202300515>

the electrochemical performance of the battery. Carbonaceous materials with amorphous morphology are known to deliver high-rate performance and thus exhibit higher power density.^[14] Due to the disordered arrangement of carbon layers, a predominant capacitive behaviour is exhibited by amorphous carbonaceous materials. Higher capacitive behaviour lowers the charge transfer barrier and improves the kinetics of the battery.^[15] However, due to higher exposed surface area, the probability of parasitic side reactions also increases leading to lower capacity retention during cycling. On the other hand, crystalline materials exhibit diffusive behaviour and deliver a stable cycling performance with relatively higher capacity retention.^[16] However, due to longer diffusion lengths, kinetics of the battery are observed to be slower. Thus, in the application of N-doped carbon anodic active materials, the morphological factors like extent of graphitisation, crystallite size, inter layer spacing show a great impact.

From the lithium-ion storage perspective, apart from reversible capacity other factors like coulombic efficiency and energy efficiency play a significant role.^[17] Though many works are reported on N-doped carbon materials as anodes for lithium-ion batteries with high reversible capacity and cyclability, discussion on energy efficiency of those batteries is rarely presented. Despite a high columbic efficiency, it is tougher to get a higher energy efficiency. Energy efficiency is the ratio of charge energy to discharge energy.^[18] Lower energy efficiency indicates that some amount of energy is being converted to different forms like thermal energy leading to heating up of the battery or can cause undesirable side reactions.

In this work, a novel single source of carbon and nitrogen i.e., BIAN-Melamine based porous organic polymer was employed to synthesise N-doped carbon. The synthesis has been carried out at three different temperatures i.e., 600° (labelled as PyPBM600), 700° (labelled as PyPBM700), 800° (labelled as PyPBM800) and effect on morphology has been presented. PyPBM600 was found to be relatively more amorphous and exhibited higher capacitive behaviour with lower capacity retention in charge and discharge studies. The scope of this study is to understand the effect of temperature on the nitrogen doping in the carbon and morphology of the carbon. Aurora et al., have shown that at lower temperatures (such as 600°C), major fraction of carbon will be in the form of amorphous carbon because of insufficient energy available for graphitisation. As the temperatures are increased ($\geq 800^\circ\text{C}$) defects are decreased due to the availability of sufficient activation energy. Hence in this study two temperatures namely, 600°C and 800°C were chosen to obtain hard carbon with different morphologies and nitrogen content. If the temperature is increased further to $\geq 1000^\circ\text{C}$, the extent of graphitisation increases, which leads to the increase in intercalative charge storage. This hinders the fast-charging ability of the active material. In this context, 600°C and 800°C were chosen to obtain hard carbon morphology with significant amorphous nature leading to capacitive behaviour. Higher capacitive contribution decreased the activation energy for charge transfer which was found to be 33.43 kJ/mol. Whereas PyPBM800 exhibited relatively more crystallinity and found to

exhibit a significant diffusive behaviour too. The inclusion of bulk contribution led to the increase in activation energy for charge transfer, which was evaluated to be 33.69 kJ/mol. Furthermore, the electrochemical behaviour of both the materials in terms of reversible capacity, rate capability, cyclability, redox behaviour and charge transfer kinetics has been presented in detail and a comparison has been brought out. Full cells were fabricated using PyPBM600 and PyPBM800 as anodic active materials. Full cell prepared with PyPBM800 active material as anode and LiNCAO ($\text{LiNi}_{0.8}\text{Co}_{0.15}\text{Al}_{0.05}\text{O}_2$) cathode delivered a reversible capacity of 1.2 mAh at 15-minute charging time, with an energy efficiency of 90% and specific energy of 325 Wh/kg at material level.

Results and discussion

X-ray diffraction (XRD) studies have been conducted to understand the morphologies of PyPBM600, PyPBM700 and PyPBM800 (Figure 1a, 1b). XRD of PyPBM600 shows a relatively broad peak with a FWHM of 5° centred at 25.7° corresponding to an interlayer spacing of 0.346 nm. XRD of PyPBM800 shows a relatively less broad peak with a FWHM of 2.7° centred at 26.2° corresponding to an interlayer spacing of 0.340 nm. The FWHM values of three samples indicate PyPBM800 is relatively more arranged. Crystalline fraction was calculated as described by Jae-Seung Roh et al^[19] (Figure S1). The crystalline fraction in PyPBM600 was evaluated to be 51.3% whereas in the case of PyPBM800 it was found to be 61.6%. Further to estimate the extent of stacking, R- factor was calculated (Figure S2). R factor was evaluated to be 2.33 in PyPBM600 and 2.67 in PyPBM800 indicating higher number of parallelly arranged carbon sheets in PyPBM800 than in PyPBM600 which further strengthens the observation of PyPBM800 being relatively more crystalline. These results indicate that upon pyrolysis till 800°C a relatively more crystalline morphology is obtained than 600°C. Further crystallite size has been evaluated using the FWHM value of XRD pattern. Crystallite size refers to the coherently diffracting volume in the material resulting in the diffraction pattern. The following equation was used to calculate the crystallite size:^[20]

$$\tau = \frac{K \lambda}{\beta \cos\theta} \quad (1)$$

where τ is the mean size of the ordered (crystalline) domains, K is a dimensionless shape factor with a value close to unity, λ is the X-ray wavelength, β is the line broadening at half the maximum intensity (FWHM) and Θ is the Bragg angle. The average crystallite size of PyPBM600 was calculated to be 1.7 nm, and PyPBM800 to be 3.2 nm. PyPBM800 sample with relatively better crystalline structure as understood from crystalline fraction, crystallite size and R-factor can be expected to exhibit significant diffusive charge storage mechanism whereas PyPBM600 with relatively more anisotropy, can be expected to exhibit a predominant capacitive behaviour.^[6] With the basic understanding on the morphology of PyPBM600 and PyPBM800 using X-ray Diffraction (XRD), High resolution trans-

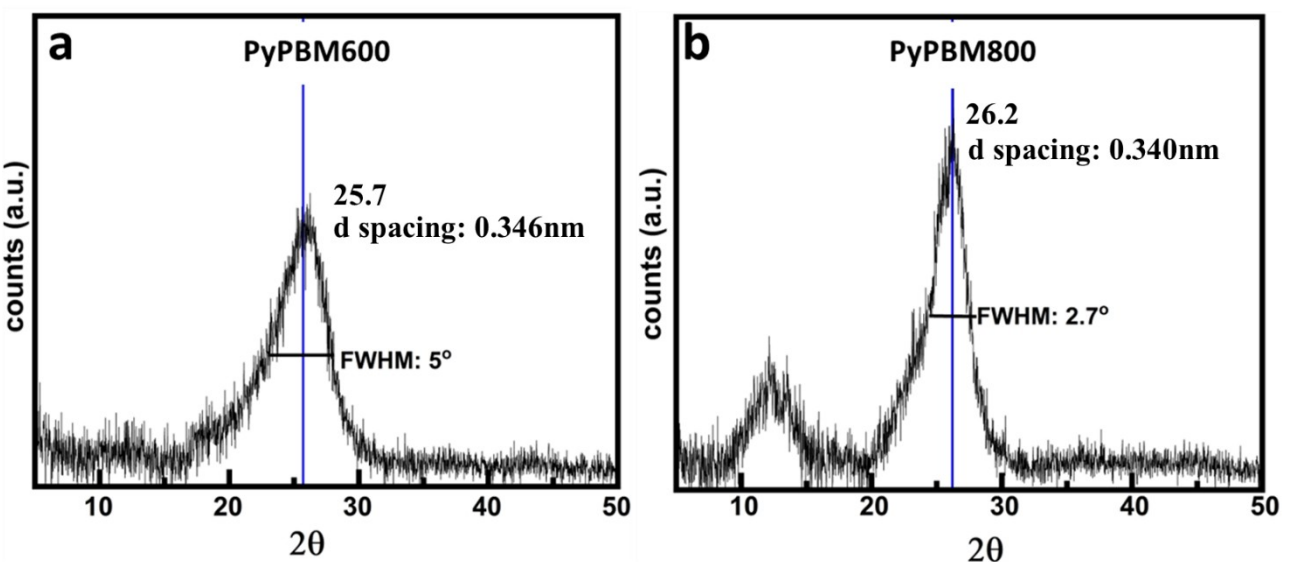
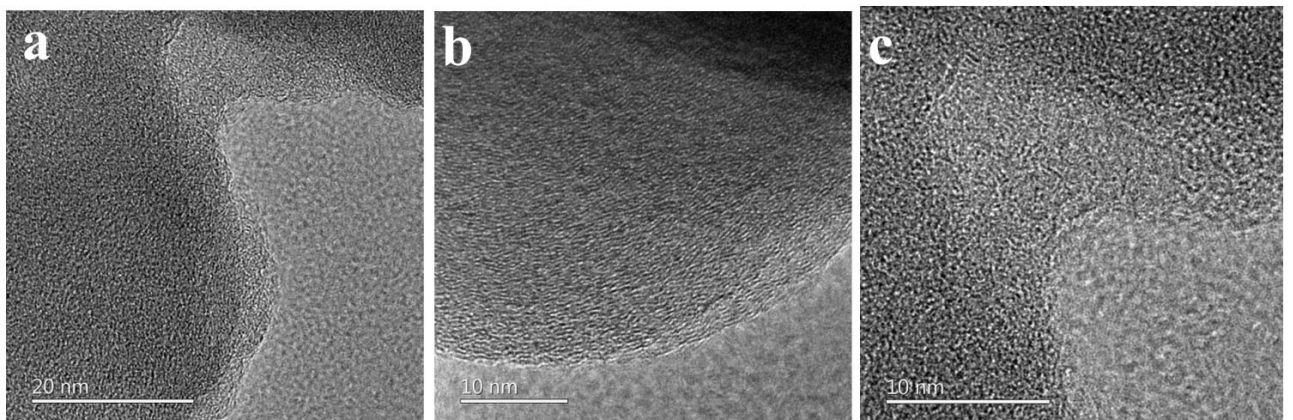


Figure 1. a) XRD of PyPBM600 b) XRD of PyPBM800.

mission electron microscopy (HRTEM) imaging has been conducted. Figure 2 shows HRTEM images of PyPBM600 and PyPBM800. PyPBM600 exhibits a layered but turbostratic structure as seen in images 2a and 2b. Whereas PyPBM800 shows a relatively less turbostratic structure (Figures 2d and 2e). Using inverse Fast Fourier Transform (FFT) of the HRTEM image taken at 10 nm resolution (Figure S3), d-spacing was calculated for PyPBM600 to be 0.35 nm and that in case of PyPBM800 (Figure S4) was found to be 0.34 nm. In both the cases, the d-spacing value was found to be in agreement with XRD. As mentioned earlier, relatively more distorted structure can lead to more surface controlled capacitive contribution and in the latter case, a significant contribution from bulk controlled diffusion process can be expected. HRTEM- energy dispersive X-Ray analysis (EDX) of PyPBM600 and PyPBM800 showed uniform distribution of carbon (Figures S5a and S5c) and nitrogen (Figures S5b and S5d) highlighting the benefit of using a single source of carbon and nitrogen. As carbon and nitrogen are uniformly distributed in the precursor polymer, same distribution has been retained in the carbonaceous material too. Another important factor leading to fast charging is defects in the framework of the anode. To gain understanding of the defects present in both the materials, Raman spectroscopy has been conducted (Figure 4a, b). Raman spectroscopy indicated higher degree of induced defects in both all three samples. The I_d/I_g ratio in the case of PyPBM600 (Figure 3a) was found to be 0.99 and in the case of PyPBM800 (Figure 3b) was found to be 0.90 indicating slightly higher defects in PyPBM600. In the Raman spectra of PyPBM800, relatively higher intensity of 2D band was observed indicating comparatively better layered arrangement in PyPBM800.^[21] Figures S6a and S6b show the BET isotherms of PyPBM600 and PyPBM800. The surface area of PyPBM600 was found to be $29.5 \text{ m}^2/\text{g}$ and PyPBM800 was found to be $17.7 \text{ m}^2/\text{g}$. The higher surface area of PyPBM600 is due to its higher amorphous content and higher degree of induced

defects than in case of PyPBM800. Figures S6c and S6d show the Thermogravimetric Analysis (TGA) and Differential Thermal Analysis (DTA) profiles of PyPBM600 and PyPBM800 in air. Irrespective of the differences of micro crystallinity, both the materials showed similar TGA profile, with oxidation onset at 425°C . DTA profile showed similar area under curve for both PyPBM600 and PyPBM 800, indicating that the enthalpy change in the oxidation process is same for both the materials. This implies that the minor differences in the morphologies of PyPBM600 and PyPBM800 did not have a significant effect on the extrinsic property like enthalpy. Following the studies on morphological characteristics, to understand elemental composition, EDX was conducted (Figures S7a and S7b). The atomic percentage (Table S1) of carbon in PyPBM600 was found to be 78.82% corresponding to a weight percentage of 75.32% and a high nitrogen atomic content of 14.35% corresponding to a weight percent of 15.99%. Further, 6.8 atom percentage of oxygen was detected due to the adsorbed CO_2 on the sample corresponding to a weight percentage of 8.69%. Similarly, in PyPBM800, atomic percentage (Table S2) of carbon was found to be 88.24% corresponding to a weight percentage of 86.02% and a nitrogen content of 8.0% corresponding to a weight percent of 9.09%. Further, 3.7 atom percentage of oxygen was detected due to the adsorbed CO_2 on the sample corresponding to a weight percentage of 4.8. X-ray photoelectron spectroscopy (XPS) was conducted to precisely understand various functional groups present in PyPBM600 and PyPBM800. Survey spectra showed peaks corresponding to carbon, nitrogen and oxygen (Figures S8a, S9a). The deconvoluted C1s XPS spectra of PyPBM600 (Figure S8b) shows peaks at 284.6 eV, 285.59 eV, 287.98 eV corresponding to $\text{C}=\text{C}$, $\text{C}=\text{N}/\text{C}-\text{N}$ and $\text{C}=\text{O}$ groups respectively.^[22] The deconvoluted N1s spectra (Figure 3c) shows two peaks at 398.48 eV and 399.68 eV corresponding to pyridinic and graphitic nitrogen respectively. Further, using the following formula,^[3]

PyPBM600



PyPBM800

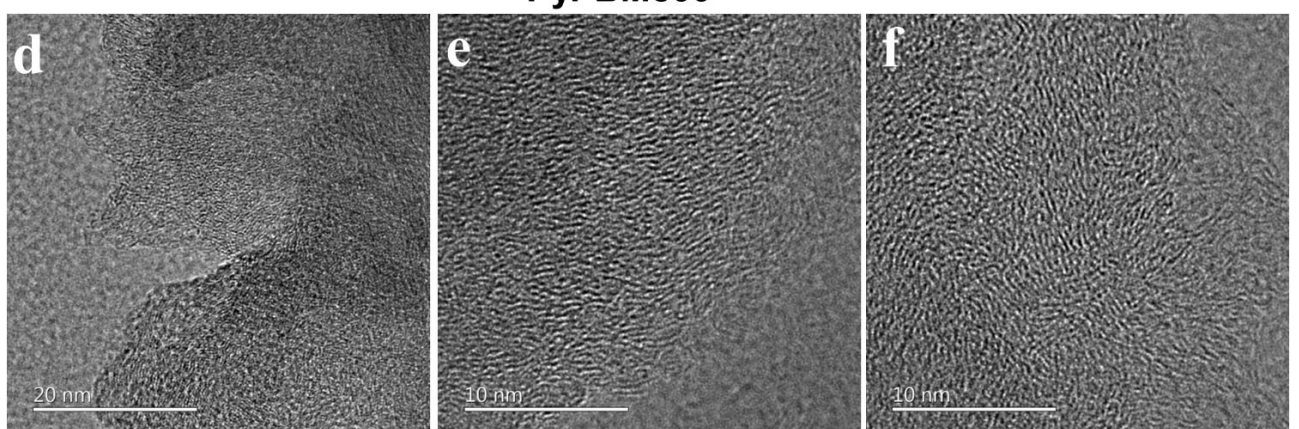


Figure 2. a, b, c TEM images of PyPBM600 at 20 nm, 10 nm and 10 nm; d, e, f TEM images of PyPBM800 at 20 nm, 10 nm and 10 nm.

$$\text{Atomic percentage} = \frac{\frac{\text{area of the peak}}{\text{sensitivity factor}}}{\sum \frac{\text{area}}{\text{sensitivity factor}}} \times 100 \quad (2)$$

From the above formula, the atomic percentage of nitrogen was found to be 14%. Which is like the observation made in EDX spectra. Among the nitrogen content present, 63% is in the form of graphitic nitrogen and 37% is in the form of pyridinic nitrogen. The relatively high amount of nitrogen in the sample suggests a better electrochemical performance as discussed earlier. The deconvoluted C1s XPS spectra of PyPBM800 (Figure S9b) shows peaks at 284.6 eV, 286.3 eV, 286.9 eV corresponding to C=C, C=N/C–N and C=O groups respectively. The deconvoluted N1s (Figure 3d) spectra shows two peaks at 398.46 eV and 400.5 eV corresponding to pyridinic and graphitic nitrogen respectively.^[23] Further, using equation 2, the atomic percentage of nitrogen was found to be 10%. Which is similar to the observation made in EDX spectra. Among the nitrogen content present, 67% is in the form of graphitic nitrogen and 33% is in the form of pyridinic nitrogen. In the analysis of XRD it was found that the crystallinity increases with temperature. David et al., reported the synthesis of N-doped CNTs at different temperatures. It was found that the materials with lower

crystallinity and higher degree of induced defects are more prone to form C–N bond. Further, C–N bond energy is 305 kJ/mol and C–C bond energy is 370 kJ/mol. This indicates that at lower temperatures, C–N bond formation is easier. At higher temperatures, C–C is more favourable. Furthermore, another possible reason is the formation of stable N₂, which is liberated from hard carbon framework. Hence, though the source of PyPBM 600 and PyPBM800, the difference in synthetic temperature leads to the difference of nitrogen content. Further, Cao et al., demonstrated from first principles study that pyridinic nitrogen can improve the reversible capacity of LiBs significantly because of the structural defects.^[24] Higher content of pyridinic nitrogen, higher degree of induced defects, lower crystallinity in PyPBM600 may lead to higher capacitive contribution in addition to its relatively more turbostratic nature.^[25] To confirm the effect of temperature, N-doped carbon was synthesised at an intermediate temperature of 700 °C as well. From the analysis of XRD and Raman spectrum (Figure S11), it was found that PyPBM700 has intermediate crystallinity in comparison to PyPBM600 and PyPBM800 (Figures S1, S2). Also, the nitrogen content was found to be 12% (Figure S10) which is intermediate to PyPBM600 and PyPBM800 strengthening the understanding about temperature effect on

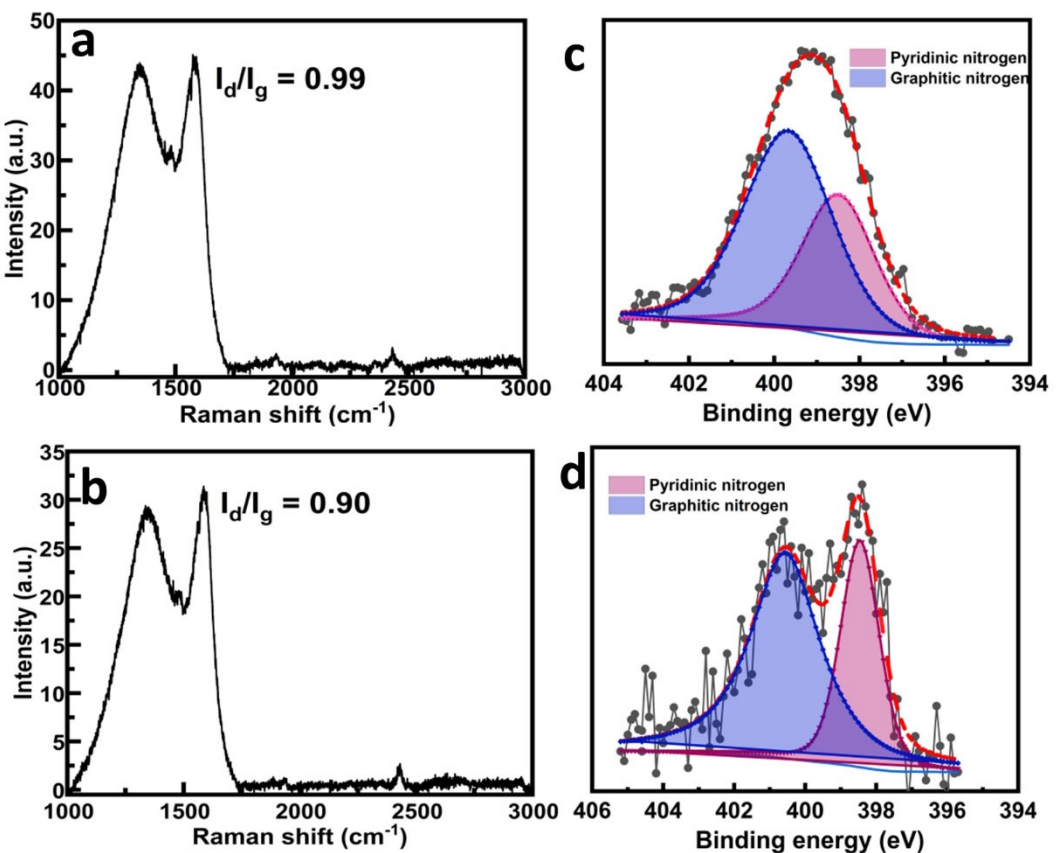


Figure 3. a) Raman spectrum of PyPBM600 b) Raman spectrum of PyPBM800 c) N1s XPS spectrum of PyPBM600 d) N1s XPS spectrum of PyPBM800.

nitrogen. These results validate the correlation between temperature, morphology and nitrogen content.

Following the morphological and functional group elucidation, cyclic voltammetry was conducted to gain insights into the redox behaviour of PyPBM600 and PyPBM800 (Figure S12a and S12c). In the cyclic voltammograms of both anodic half-cells with PyPBM 600 and PyPBM800 as active materials (hereafter referred to as PyPBM600 half-cell and PyPBM800 half-cell for simplicity), no defined lithiation and delithiation peaks were observed which is a characteristic of turbostratic materials. An irreversible reduction peak at 0.65 V was observed in both the cyclic voltammograms due to the reduction of electrolyte leading to formation of solid-electrolyte interphase (SEI). To understand the effect of SEI, Potentiostatic electrochemical impedance spectroscopy (PEIS) has been conducted before and after cyclic voltammetry. After cyclic voltammetry, due to the formation of SEI layer, the anode resistance was found to decrease drastically in both PyPBM600 (Figure 4a) and PyPBM800 (Figure 4b) half-cells ascertaining the formation of SEI.^[26] Yamada et al., reported that the de-solvation of lithium ions at the electrode-electrolyte interface is a probable rate limiting step in the kinetics of lithium-ion battery^[27] and is a major contributing factor to impedance.^[28] Since one of the functional properties of SEI layer is to help in de-solvation of lithium ions at the electrolyte-SEI interface,^[29,30] the decrease in impedance after cyclic voltammetry is observed as shown in Figures 4a and 4b and Table S3. Elaborate details on the SEI resistance, components and

approximate thickness of SEI are discussed in later sections. Further, the activation energies for desolvation in PyPBM600 and PyPBM800, the following equation was employed:^[31]

$$\ln\left(\frac{1}{R_{CT}}\right) = \ln A + \left(\frac{-E_a}{R}\right)\left(\frac{1}{T}\right) \quad (3)$$

(Where, R_{CT} is charge transfer resistance, A is pre-exponential factor, E_a is activation energy, R is universal gas constant and T is temperature). PEIS was conducted at lithiation potential of both PyPBM600 and PyPBM800 at 30°, 40°, 50° and 60° (shown in Figures S14a, S15a). Linear plot of $\ln(1/R_{CT})$ and $(1/T)$ was used to calculate activation energies (E_a) (Figures S14b, S15b). The E_a of PyPBM600 half-cell was evaluated to be 33.44 kJ/mol and 33.69 kJ/mol in PyPBM800 half-cell. The E_a in case of PyPBM600 was found to be lower than in case of PyPBM800 indicating the possibility of easier charge-transfer in PyPBM600 half-cell. It is to be noted that minor increase in the micro crystallinity of PyPBM 800 led to significant difference in the activation energy. From the same plot, preexponential factor, also known as the frequency factor which indicates the number of collisions taking place between the reactants per second, was evaluated to be $45 \times 10^3 \text{ sec}^{-1}$ for PyPBM600 half-cell and in the case of PyPBM800 half-cell it was evaluated to be $14 \times 10^3 \text{ sec}^{-1}$. Higher frequency factor indicates higher number of collisions approaching the activation energy barrier in case of PyPBM600, suggesting ease of

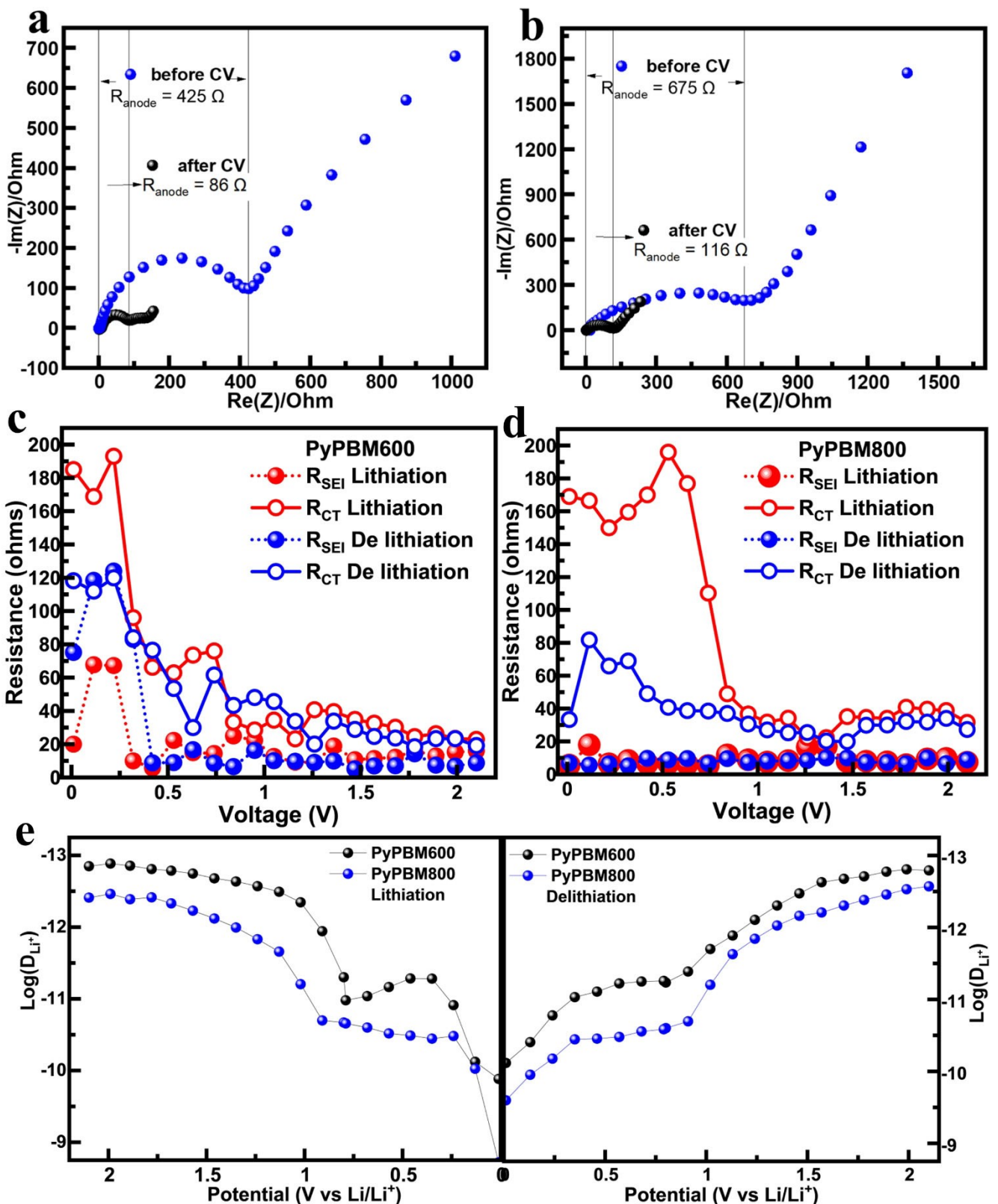


Figure 4. a) PEIS of anodic half-cell with PyPBM600 as anodic active material b) PEIS of anodic half-cell with PyPBM800 as anodic active material c) R_{CT} and R_{SEI} of PyPBM600 half-cell during lithiation and delithiation d) R_{CT} and R_{SEI} of PyPBM800 half-cell during lithiation and delithiation e) lithium-ion diffusion coefficient in PyPBM600 and PyPBM800 at various potentials during lithiation and de-lithiation.

lithiation. From the charge-transfer resistance values, the exchange current density (j_o) i.e., the rate of transfer of electrons or charges between electrode and electrolyte under dynamic equilibrium is estimated using the following formula:^[32]

$$j_o = \frac{RT}{nFAR_{CT}} \quad (4)$$

Where, j_o is exchange current density, R is universal gas constant, T is temperature in kelvin, n is number of electrons transferred, F is faradays constant, A is area of electrode and R_{CT} is charge-transfer resistance. Higher the j_o value, easier is the reaction to initiate. The j_o value of PyPBM600 was found to be 8.8×10^{-4} mA/cm² and in case of PyPBM800 to be 3.4×10^{-4} mA/cm². Higher j_o in PyPBM600 affirms the previous observation of faster charge transfer in PyPBM600. As mentioned earlier, resistances from SEI and charge-transfer play a crucial role in the kinetics of lithium-ion battery. To quantify these resistances, dynamic electrochemical impedance spectroscopy was conducted in the potential range of 10 mV to 2.1 V. Figures S16a, S16b show dynamic electrochemical impedance spectroscopy (DEIS) of PyPBM600 half-cell and Figures S17a, S17b show DEIS of PyPBM800 half-cell. The DEIS profiles of PyPBM600 and PyPBM800 show typical behaviour i.e., a semicircle in the high frequency region followed by a straight line in the low frequency region. In this context, it must be noted that in the earlier sections, the charge storage was found to be capacitive in nature. A typical double layer capacitor has 90° straight line in the low frequency region^[33] i.e., does not have any component behaving as resistor in the low frequency region. Whereas the EIS spectra of PyPBM600 and PyPBM800 show a significant real impedance in the low frequency region too. This indicates that capacitance here includes charge transfer and diffusion and hence must be considered as intercalative pseudo capacitance materials. SEI resistance and charge-transfer resistance were obtained by equivalent circuit analysis^[34] (circuit shown in Figures S14c, S15c). Charge-transfer resistance was observed to be lower in PyPBM600 (shown in Figure 4c) than PyPBM800 (shown in Figure 4d) in both lithiation and delithiation. SEI resistance (Figure 4c and 4d) was found to be higher in case of PyPBM600 half-cell than PyPBM800 half-cell. As observed previously, the morphology of PyPBM600 is amorphous and correspondingly, the R_{CT} is lower, and j_o is higher. This indicates, higher reactivity towards electrolyte. Excessive electrolyte reduction causes thicker SEI and low-capacity retention. Further charge transfer resistance, in both the half-cells was observed to be higher in case of lithiation than in delithiation. During lithiation, lithium-ion concentration decreases in the electrolyte and increases in anode. Decrease in number of ions in electrolyte lowers the exchange current density (j_o). Recall from equation 4, that j_o has an inverse dependence on charge-transfer resistance. Lower exchange current density implies higher charge transfer resistance.^[35] Further, as seen in the dQ/dV plots of PyPBM600 and PyPBM800 half-cells (Figures S18b, S18d) maximum lithiation of anode occurs in the potential range of 10 mV to 1.0 V. This implies a decrease in the lithium-ion concentration in the electrolyte and lower j_o and higher R_{CT} . Also, it is important to note that the charge transfer resistance values presented in the PEIS at OCP differs from the

charge resistance in DEIS values at same potential. In DEIS, the applied current is large, causing overpotential. From butler-Volmer equation (equation S1), we know that the charge-transfer resistance is inversely related to overpotential. Therefore, the difference in R_{CT} between PEIS and DEIS is unavoidable.^[36] With this understanding on R_{CT} , R_{SEI} at high frequencies, lithium-ion diffusion has been evaluated with the impedance data obtained at lower frequencies using the following Warburg equation:^[37]

$$D_{Li^+} = \frac{R^2 T^2}{2A^2 n^4 F^4 C^2 \sigma^2} \quad (5)$$

Where R is universal gas constant, T is temperature in kelvin, A is area of the electrode (cm²), n is number of electrons transferred, F is faradays constant, C is concentration of electrolyte and σ is Warburg coefficient. Warburg coefficient is evaluated using the following equation:^[34]

$$Z_{real} = (R_{Electrolyte} + R_{CT}) + \sigma\omega^{-0.5} \quad (6)$$

Where Z_{real} is real impedance and ω is angular frequency. Figure 4e shows the diffusion coefficient of PyPBM600 and PyPBM800 at different potentials. It can be observed that the diffusion coefficient of PyPBM800 is higher than that of PyPBM800 in the potential range of 10 mV to 2.1 V.

Following cyclic voltammetry and impedance studies, galvanostatic charge and discharge studies were conducted to understand the lithium storage ability of PyPBM600 and PyPBM800. Figure 5a shows the rate studies of PyPBM600 half-cell. Reversible capacities of 425 mAh/g, 280 mAh/g, 235 mAh/g, 191 mAh/g, 172 mAh/g, 110 mAh/g, 52 mAh/g at 50 mA/g, 200 mA/g, 400 mA/g, 750 mA/g, 1000 mA/g, 2000 mA/g and 4000 mA/g respectively. Figures 5c and S18a show the long cycling studies of PyPBM600 anodic half-cell, reversible capacities of 250 mAh/g, 140 mAh/g, 120 mAh/g were observed for 2000, 1500 and 1000 cycles respectively at 1000 mA/g, 2000 mA/g and 4000 mA/g current densities respectively. The coulombic efficiency was found to be 100% for all three cells. The capacity retention was found to be 90% for 2000 cycles, 82% for 1500 cycles and 79% for 1000 cycles at 1000 mA/g, 2000 mA/g and 4000 mA/g respectively. Figure 5b shows the rate studies of PyPBM800 half-cell. Reversible capacities of 440 mAh/g, 365 mAh/g, 252 mAh/g, 200 mAh/g, 177 mAh/g, 122 mAh/g, 65 mAh/g were observed at 50 mA/g, 200 mA/g, 400 mA/g, 750 mA/g, 1000 mA/g, 2000 mA/g and 4000 mA/g respectively. Figures 5d and S18c show the long cycling studies of PyPBM800 anodic half-cell, reversible capacities of 260 mAh/g, 105 mAh/g, 86 mAh/g were observed for 500, 1500 and 2000 cycles respectively at 1000 mA/g, 2000 mA/g and 4000 mA/g current densities, respectively. The coulombic efficiency was found to be 100% for all three cells. The capacity retention was found to be 91% for 500 cycles, 92% for 1500 cycles and 99% for 2000 cycles at 1000 mA/g, 2000 mA/g and 4000 mA/g respectively. The reversible capacity obtained by the anodic half-cells with PyPBM600 active material is higher than that of anodic half-cells with PyPBM800 active material. However, the capacity retention of the anodic half-cells is poor, which

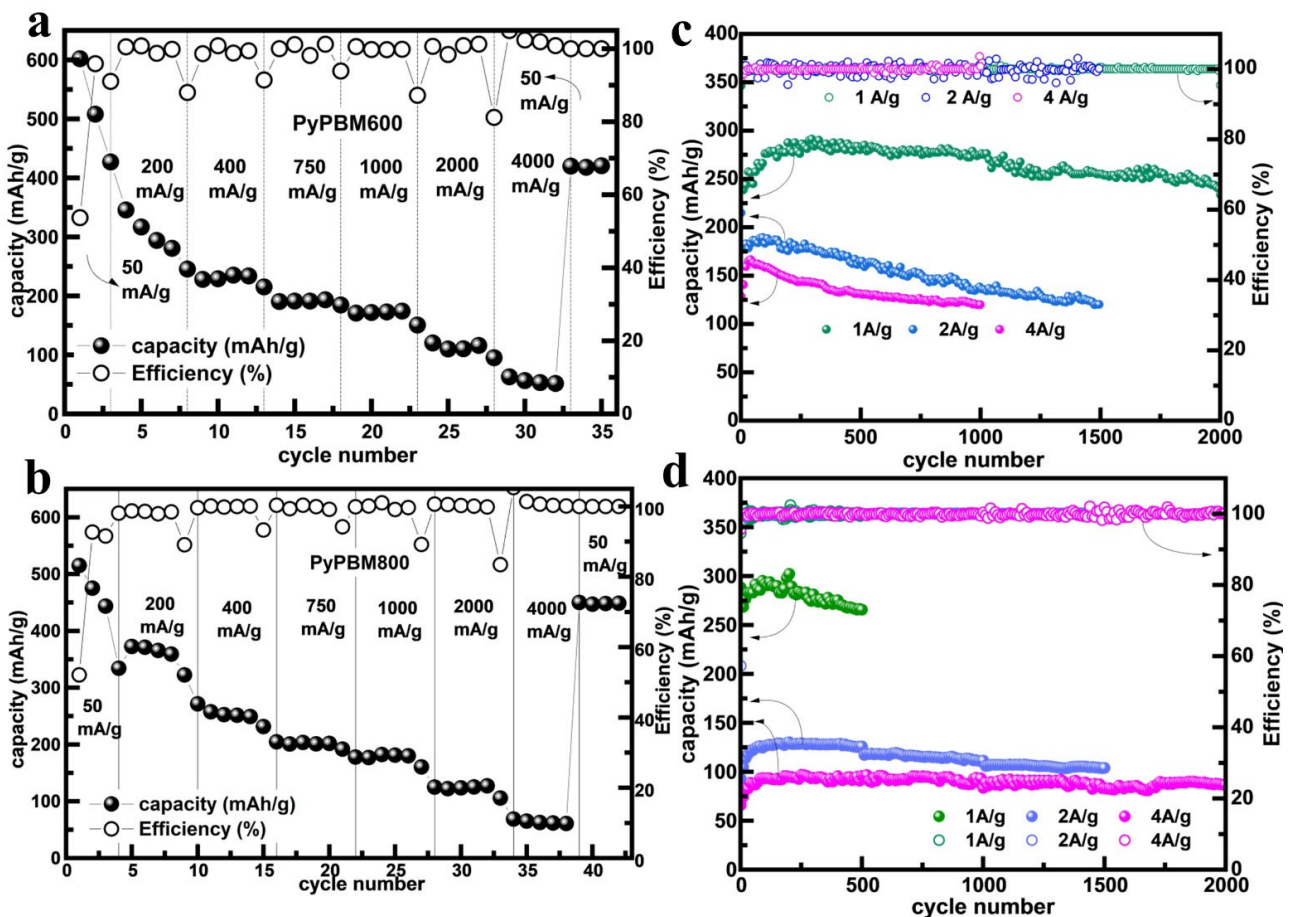


Figure 5. a) Rate studies of PyPBM600 anodic half-cell b) Rate studies of PyPBM800 anodic half-cell c) Long cycling studies of PyPBM600 half-cell at 1 A/g, 2 A/g, and 4 A/g d) Long cycling studies of PyPBM800 half-cell at 1 A/g, 2 A/g, and 4 A/g.

indicates that there is irreversible capacity loss. As discussed earlier, relatively more turbostratic nature and higher nitrogen content led to better rate performance by PyPBM600 half-cell than PyPBM800 half-cell. To further confirm this observation, charge-discharge studies of PyPBM700 half-cells were conducted (Figure S19). At 4 A/g, a reversible capacity of 105 mAh/g was obtained with a retention of 91%. The capacity and retention values were observed to be intermediate to PyPBM600 and PyPBM800, validating the effect of temperature on capacity and retention. Furthermore, due to the difference in morphology and nitrogen content, activation energy was found to be lower in PyPBM600 and the frequency factor and exchange current density were found to be higher in PyPBM600. This indicates the possibility of fast charging and better rate capability. However, this can also lead to irreversible capacity loss through SEI growth. From equation 0, the length of diffusion in case of anodic half-cells with PyPBM600, PyPBM800 and graphite (comparison) as anodic active materials (Table S4). In comparison with graphite, PyPBM600 and PyPBM800 were found to be exhibiting shorter length of diffusion and among PyPBM600 and PyPBM800, higher diffusion coefficient in PyPBM800 led to shorter length of diffusion.

It must be taken into consideration that in practical application of a battery, unlike a half-cell with very high lithium ions available

due to having lithium foil as counter electrode, full cell with a limited lithium source like LiCoO₂ is used. In this context, capacity retention plays a crucial role as lithium inventory loss cannot be afforded in the battery. Hence, in a wholistic perspective, despite a slightly lower reversible capacity, PyPBM800 offers a better prospective due to its good capacity retention. After charge-discharge studies, anodic half cells were decrimped under Ar atmosphere (O₂ and H₂O < 0.5 ppm) and the PyPBM600 and PyPBM800 electrode surfaces were analysed using XPS. The deconvoluted C 1s spectra of cycled PyPBM600 anode (Figure S20a) showed peaks at 283.8 eV, 284.6 eV, 285.3 eV, 286.1 eV, 287 eV and 289.4 eV corresponding to C-Li, C=C, C=N/C-N, C=O, C—O—C and Li₂CO₃ respectively. The N 1s spectra of cycled PyPBM600 anode (Figure S20b) showed peaks at 397.8 eV and 399.8 eV corresponding to N-Li and C=N respectively. The O 1s spectra of cycled PyPBM600 anode (Figure S20c) showed peaks at 530.3 eV, 531.0 eV, 531.9 eV and 533.0 eV corresponding to C=O, C—O—C, Li₂CO₃ and Li₂O. The P 1s spectra of cycled PyPBM600 (Figure S20d) showed a peak at 136.5 eV corresponding to Li_xPF_y. The XPS results suggest that Li₂CO₃, Li₂O and Li_xPF_y are the components of SEI in case of cycled PyPBM600 electrode. The C 1s spectra of cycled PyPBM800 anode (Figure S21a) showed peaks at 283.8 eV, 284.6 eV, 285.2 eV, 286.1 eV, 287.2 eV and 289.4 eV corresponding to C-Li, C=C, C=N/C-N, C=O, C—O—C and Li₂CO₃.

respectively. The N 1s spectra of cycled PyPBM800 anode (Figure S21b) showed a single peak at 399.5 eV corresponding to N–Li. The O 1s spectra of cycled PyPBM800 anode (Figure S21c) showed peaks at 531.0 eV, 531.8 eV and 532.8 eV corresponding to C–O–C, Li_2CO_3 and Li_2O . The P 1s spectra of cycled PyPBM800 (Figure S21d) showed a peak at 137.5 eV corresponding to Li_xPF_y .^[38] From the postmortem XPS studies, the components of SEI of PyPBM800 anodes were found to be Li_2CO_3 , Li_2O , Li_xPF_y . Further, kinetic studies were conducted to understand the mechanism of charge storage. Figure 6a and 6b show the cyclic voltammograms at various scan rates of PyPBM600 half-cell and PyPBM800 half-cell. PyPBM600 half-cell shows higher overpotential

than PyPBM800 half-cell. It was also observed that the peak current and scan rates follow a linear dependence. The linear fit of their logarithmic plots (Figure S22, S23) showed a slope value of 0.91 for PyPBM600 indicating a predominant capacitive contribution (Figure 6c) and 0.81 for PyPBM800 indicating a balanced capacitive and diffusive contribution^[39,40] (Figure 6d). The slope value in the linear fit of peak current and scan rate indicates the diffusive or capacitive behaviour of the material. In case of bulk controlled diffusive mechanism, the slope value would be 0.5. In case of surface controlled capacitive mechanism, the slope value would be 1.0. Quantitatively at each scan rate, a predominantly capacitive behaviour was observed in PyPBM600 half-cell. Whereas

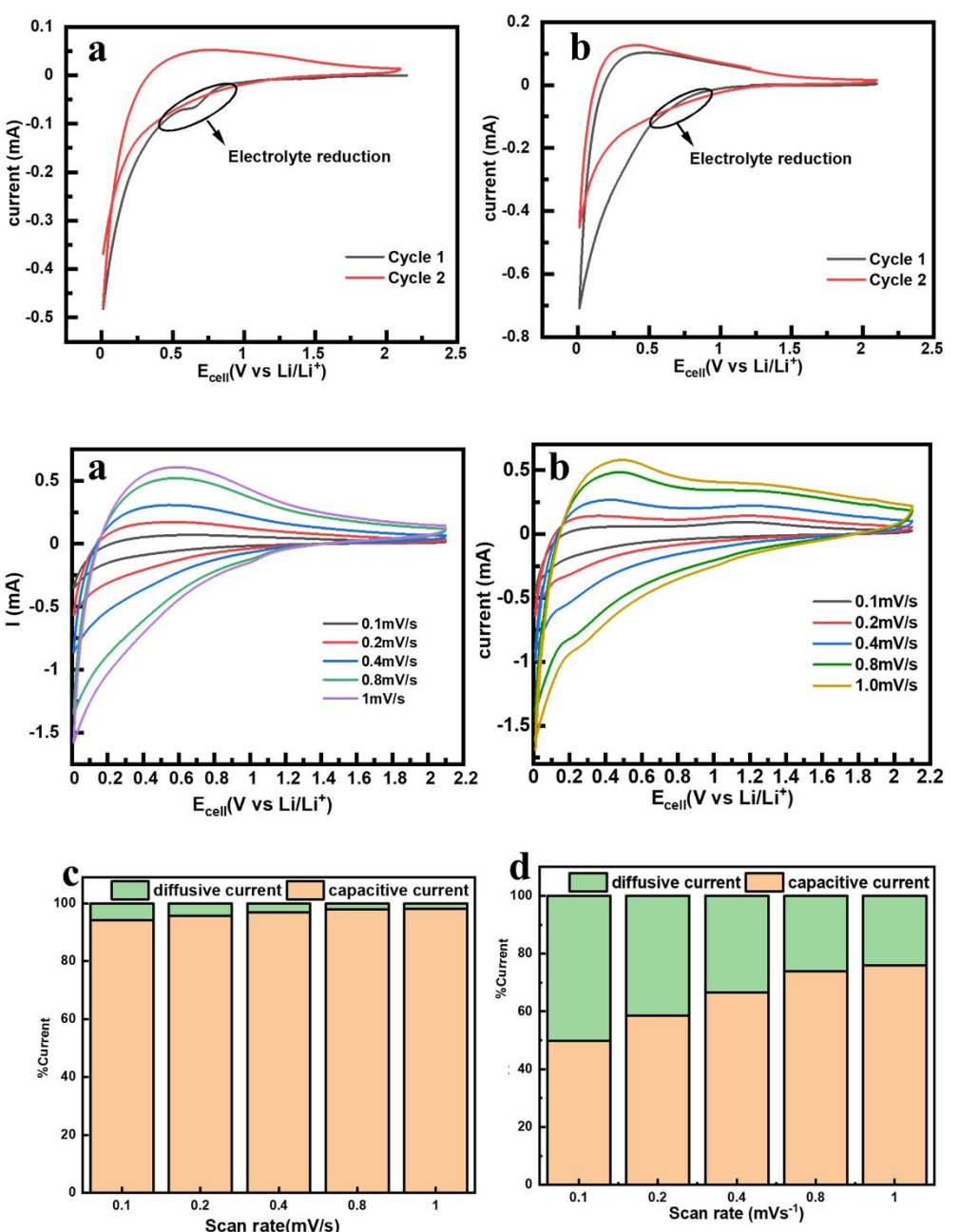


Figure 6. a) Cyclic voltammogram of PyPBM600 half-cell at different scan rates b) Cyclic voltammogram of PyPBM800 half-cell at different scan rates c) Capacitive and diffusive current distribution in PyPBM600 half-cell d) Capacitive and diffusive current distribution in PyPBM800 half-cell.

a significant diffusive behaviour is also seen in PyPBM800 half-cells at each scan rate. Hence, the initial explanation of relatively higher turbostratic nature of PyPBM600 leading to a predominant capacitive behaviour and relatively ordered nature of PyPBM800 leading to a balanced capacitive and diffusive behaviour is validated by these results.^[41]

Further, intrigued by the rate performance of PyPBM600 and PyPBM800, full cells were fabricated using PyPBM600/PyPBM 800 as anode (mass loading $\approx 8.0 \text{ mg/cm}^2$) and LiNCAO ($\text{LiNi}_{0.8}\text{Co}_{0.15}\text{Al}_{0.05}\text{O}_2$) as cathode. Charge and discharge studies of full cell with PyPBM600 anode (Figures 7a, S24a) showed a reversible capacity of 0.9 mAh at 0.5 mA/cm^2 current density after 50 cycles with a coulombic efficiency of 99.7%. The capacity retention was observed to be 60% after 50 cycles. At the same current density, full cell with PyPBM800 anode delivered a reversible capacity of 1.6 mAh with a capacity retention of 85% for 50 cycles (Figure 7d, S24b). These results suggest better performance of PyPBM800 anode in full cell environment. To further understand the performance of full cell with PyPBM800 anode, charge and discharge studies at various current densities (Figure 7c) were conducted. The full cell with PyPBM800 anode showed a good reversible capacity of 1.7 mAh at 0.06 mA/cm^2 , 1.6 mAh at 0.15 mA/cm^2 , 1.5 mAh at 0.30 mA/cm^2 , 1.4 mAh at 0.6 mA/cm^2 , 1.2 mAh at 1.2 mA/cm^2 and 1.1 mAh at 2.4 mA/cm^2 . Long cycling studies (Figure 7e) were carried out at 2.4 mA/cm^2 charging current and 0.6 mA/cm^2 discharge current. A reversible capacity of 1.2 mAh was observed for 300 cycles with a coulombic efficiency of 99.8%. The charging time at this current density was found to be (~) 15 minutes and the time of discharge was 2.5 hours. The excellent performance of the full cell with PyPBM800 anode indicates that the importance of having a balanced capacitive and diffusive properties for fast charging as

well as long cyclability. Following the excellent rate capability and cyclability of full cell with PyPBM800 anode, to determine the applicability of PyPBM800, energy efficiency (E_{eff}) was calculated using following formula:^[42,18]

$$E_{\text{eff}} = \frac{\text{Discharge capacity}}{\text{charge capacity}} \times \frac{\text{average discharge potential}}{\text{average charge potential}} \times 100 \quad (7)$$

Which can be summarised as:

$$E_{\text{eff}} = \text{Coulombic efficiency} \times \text{voltage efficiency} \quad (8)$$

Average charge/discharge potential was determined using following equation:^[43]

$$V_{\text{avg}} = \frac{1}{Q_T} \int_0^{Q_T} V dQ \quad (9)$$

Where, V_{avg} is average potential and Q_T is total capacity.

The energy efficiency of full cells with PyPBM600 (Figure 7b) and PyPBM800 (Figure 7f) anodes were evaluated to be 88% and 90% using equation 7. Full cell with PyPBM800 anode shows a higher specific energy. At 15-minute charging rate of full cell (2.4 mA/cm^2) with PyPBM800 anode, the voltage efficiency was found to be 90% with a minor increase in the average charge potential indicating the increase of internal resistance. The average discharge potential was observed to be almost constant throughout the cycling. Further, the energy efficiency was calculated to be 89.5% after 300 cycles. The higher energy efficiency of full cell with PyPBM800 anode was demonstrated. The specific energy (SE) of PyPBM800 in full cell

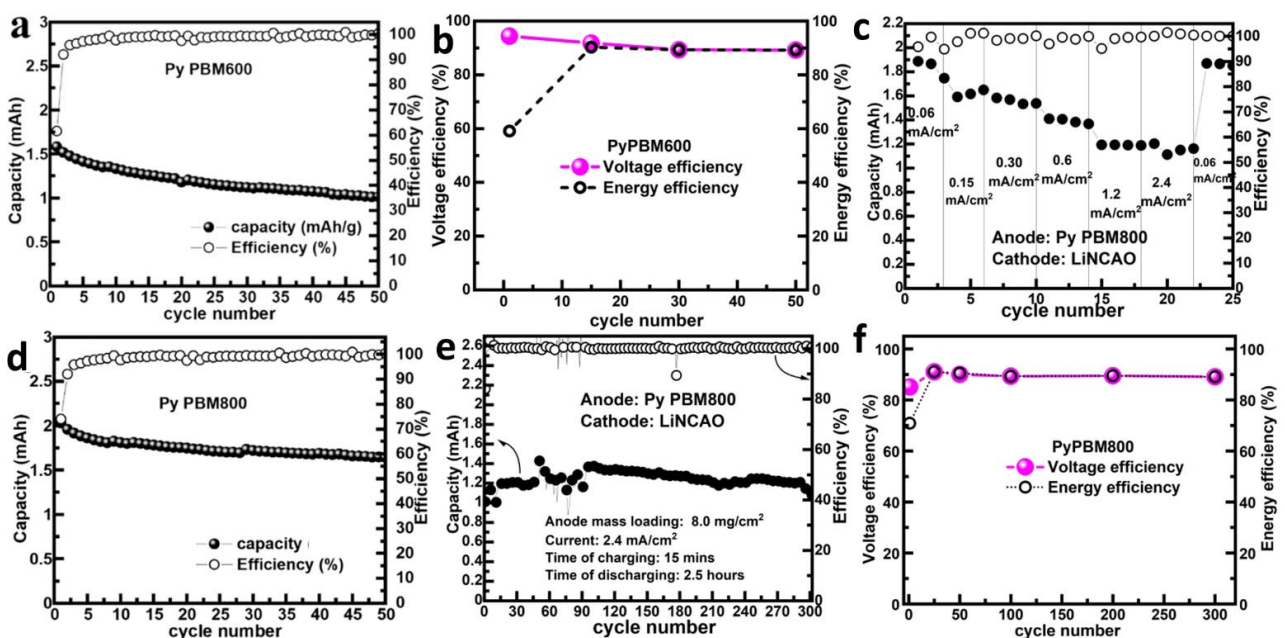


Figure 7. a) Long cycling of full cell with PyPBM600 anode b) Energy and voltage efficiencies of full cell with PyPBM600 anode c) Rate studies of full cell with PyPBM800 anode d) Long cycling of full cell with PyPBM800 anode at 0.5 mA/cm^2 e) Long cycling of full cell with PyPBM800 anode at 2.4 mA/cm^2 f) Energy and voltage efficiencies of full cell with PyPBM800 anode.

at 15-minute charging rate was evaluated to be 325 Wh/kg at material level^[44,45] using the following equation:

$$SE = \text{Gravimetric capacity} \times \text{Nominal Voltage}. \quad (10)$$

The charge-discharge results of half-cells and full-cell with PyPBM600 and PyPBM800 anodes suggest the better applicability of PyPBM800 in terms of capacity retention, rate performance and reversible capacity. This observation indicates that, in the perspective of fast charging, though amorphous materials with predominant pseudocapacitive property present an enticing option, the results demonstrated in this work suggest that besides pseudo capacitance, a significant diffusive behaviour arising from crystallinity is also essential. Hence, in the design of materials for fast charging, importance must be given both to the rate performance as well as capacity retention as ascertained by the full cell cycling data.

Conclusions

In conclusion, a single source of carbon and nitrogen namely, BIAN-melamine based porous organic polymer has been used to synthesise N-doped carbon. A novel approach towards, design of fast charging materials and their electrochemical analysis is presented in this report. The effect of synthetic conditions on the morphology of the material has been demonstrated. Pyrolysis at 800°C was found to deliver a relatively more arranged morphology of carbon. Simultaneously, in the electrochemical studies. PyPBM600 demonstrated better rate performance but poor capacity retention in comparison to PyPBM800. Table S5 shows the comparison with some earlier published reports. PyPBM800 outperforms in terms of current density, reversible capacity and cyclability. Full cell fabricated with PyPBM800 anode delivered an excellent rate capability along with a fast charging in 15 minutes with a good capacity retention and energy efficiency.

Experimental section

Materials

Acenaphthenequinone, melamine, 1,4-dioxane, mesitylene and N-methyl pyrrolidone (NMP) were bought from Tokyo chemical industries, Co.Ltd. and were used without further purification. 1.0 M LiPF₆ (50/50) ethylene carbonate/diethyl carbonate (EC/DEC) electrolyte and PVDF binder (molecular weight: 540,000) were purchased from Sigma-Aldrich. Battery-grade acetylene black was purchased from Denka Japan Private Co., Ltd. Copper foil of thickness of 20 µm was purchased from the Nilaco corporation.

Synthesis of PBM

Acenaphthoquinone (546 mg, 3 mmol) and melamine (252 mg, 2 mmol) were dispersed in about 5 mL of 1:1 1,4-dioxane and mesitylene, and 0.4 mL of acetic acid was added to the suspension. The mixture was then refluxed at 105°C for about 72 h. A dark-yellow precipitate was obtained after the reaction. The precipitate

obtained was washed with a copious amount of tetrahydrofuran (THF) and dimethylformamide (DMF) and dried at 80°C under vacuum for about 12 h. The yield obtained was about 74%. ¹H NMR (dimethyl sulfoxide (DMSO) d₆, 400 MHz) δ 8.45 (dd, J=8.3, 0.7 Hz, 2H), δ 8.05 (dd, J=6.8, 0.7 Hz, 2H), and δ 7.92 (t, J=6.9 Hz, 2H).

Synthesis of PyPBM600/PyPBM800

BIAN-melamine based porous organic polymer (PBM) was synthesized according to the procedure reported by Matsumi et al.^[46] PyPBM 600 and PyPBM800 were synthesized by pyrolyzing PBM at 600°C and 800°C, respectively. The pyrolyzed samples were ultrasonicated in deionized water to remove any amorphous carbon or carbonate impurities in the samples. The ultrasonication was followed by drying at 80°C under vacuum for about 12 hours to remove water. The samples thus obtained were ground finely using a mortar and pestle (Figure-S1).

X-ray photo electron spectroscopy. X-ray photoelectron spectroscopy (XPS) measurements were conducted on a Fisons instruments S-probe TM 2803 instrument.

Transmission electron microscopy. TEM images were acquired by scanning transmission electron microscope, JEM-ARM200F from JEOL Co.Ltd at an acceleration voltage of 200 kV.

Thermogravimetric analysis. TGA was recorded using Hitachi STA7200 thermal analysis system at a heating rate of 10°C/min and a nitrogen flow rate of 200 ml/min.

X-ray diffraction. Powder XRD studies were conducted on Smart Lab X-Ray Diffractometer, Rigaku with Cu Kα radiation ($\lambda = 0.154$ nm, over the 2θ range of 2°–45° with a step size of 0.02°).

Elemental dispersive X-ray scattering. EDX spectra were recorded in TM3030plus at 15 kV.

Electrochemical studies

Electrode preparation and cell fabrication

Py PBM600/Py PBM800, PVDF and acetylene black were taken in 8:1:1 weight ratio and the slurry was prepared in NMP using kakuhunter ball mill. The homogenous slurry thus obtained was coated on a copper foil using a doctor blade (coating thickness: 0.1 mm). The electrode was dried under vacuum at 80°C for about 12 hours and was calendared to 0.06 mm thickness at 80°C. Disks of 17 mm diameter were punched from the calendared electrode sheet. CR2025 type coin cells were fabricated in an argon filled glove box (O₂, H₂O < 0.5 ppm) using PyPBM600 or PyPBM800 electrode as anode, lithium metal foil as counter electrode, polypropylene separator (25 µm, celgard) and 1.0 M LiPF₆ (50/50) ethylene carbonate/diethyl carbonate (EC/DEC) as electrolyte. The cells were rested for about 8 hours before measurements.

Electrochemical measurements. All electrochemical measurements were performed in the potential range of 10 mV to 2.1 mV (vs Li/Li⁺) at 25°C. Cyclic voltammetry was performed in biologic VSP workstation at 0.1, 0.2, 0.4, 0.6, 0.8 and 1.0 mV/s scan rates. Potentiostatic electrochemical impedance spectroscopy was performed in a frequency range of 10 MHz to 0.1 Hz. Galvanostatic charge-discharge measurements were conducted in biologic battery cycling system at various current densities.

Supporting Information

The data that support the findings of this study are available in the supplementary material of this article. Original data are available from the authors on a reasonable request.

Additional references cited within supporting information^[47–50]

Acknowledgements

The authors are thankful to ministry of education, culture, sports and technology (MEXT), Japan for financial support and Centre for Nano Materials and Technology (CNMT) for technical support.

Conflict of Interests

The authors declare no conflict of interest.

Data Availability Statement

The data that support the findings of this study are available from the corresponding author upon reasonable request.

Keywords: N-doped carbon · Energy efficiency · Fast charging full cell · Activation energy of lithiation · Crystallite size and crystallite fraction of N-doped carbon

- [1] E. Kazyak, K. H. Chen, Y. Chen, T. H. Cho, N. P. Dasgupta, *Adv. Energy Mater.* **2022**, *12*, 1–12.
- [2] S. Nirupam Mishra, S. Punyasloka, B. Srimita Mantripragada, A. Pradhan, N. Matsumi, *ACS Appl. Energ. Mater.* **2023**, *0*, DOI 10.1021/acsaeem.3c02129.
- [3] K. S. Patnaik, R. Badam, Y. Peng, K. Higashimine, T. Kaneko, N. Matsumi, *Chem. Commun.* **2021**, *57*, 13704–13707.
- [4] P. U. Nzereogu, A. D. Omah, F. I. Ezema, E. I. Iwuoha, A. C. Nwanya, *Appl. Surf. Sci. Adv.* **2022**, *9*, 100233.
- [5] A. A. Iqbal, N. Sakib, A. K. M. P. Iqbal, D. M. Nuruzzaman, *Materialia (Oxf)* **2020**, *12*, DOI 10.1016/j.mtla.2020.100815.
- [6] S. Huang, Z. Li, B. Wang, J. Zhang, Z. Peng, R. Qi, J. Wang, Y. Zhao, *Adv. Funct. Mater.* **2018**, *28*, 1–10.
- [7] K. Kubota, S. Shimadzu, N. Yabuuchi, S. Tominaka, S. Shiraishi, M. Abreus-Sepulveda, A. Manivannan, K. Gotoh, M. Fukunishi, M. Dahbi, S. Komaba, *Chem. Mater.* **2020**, *32*, 2961–2977.
- [8] Y. Xu, Z. Li, F. Zhang, X. Zhuang, Z. Zeng, J. Wei, *RSC Adv.* **2016**, *6*, 30048–30055.
- [9] G. Lota, K. Lota, E. Frackowiak, *Electrochim. Commun.* **2007**, *9*, 1828–1832.
- [10] X. K. Kong, Q. W. Chen, *Phys. Chem. Chem. Phys.* **2013**, *15*, 12982–12987.
- [11] D. Bhattacharjya, H. Y. Park, M. S. Kim, H. S. Choi, S. N. Inamdar, J. S. Yu, *Langmuir* **2014**, *30*, 318–324.
- [12] L. Sun, L. Wang, C. Tian, T. Tan, Y. Xie, K. Shi, M. Li, H. Fu, *RSC Adv.* **2012**, 4498–4506.
- [13] K. Kubota, S. Shimadzu, N. Yabuuchi, S. Tominaka, S. Shiraishi, M. Abreus-Sepulveda, A. Manivannan, K. Gotoh, M. Fukunishi, M. Dahbi, S. Komaba, *Chem. Mater.* **2020**, *32*, 2961–2977.
- [14] K. H. Chen, V. Goel, M. J. Namkoong, M. Wied, S. Müller, V. Wood, J. Sakamoto, K. Thornton, N. P. Dasgupta, *Adv. Energy Mater.* **2021**, *11*, 1–12.
- [15] L. Fu, K. Tang, K. Song, P. A. Van Aken, Y. Yu, J. Maier, *Nanoscale* **2014**, *6*, 1384–1389.
- [16] J. Asenbauer, T. Eisenmann, M. Kuenzel, A. Kazzazi, Z. Chen, D. Bresser, *Sustain. Energy Fuels* **2020**, *4*, 5387–5416.
- [17] P. Meister, H. Jia, J. Li, R. Kloepsch, M. Winter, T. Placke, *Chem. Mater.* **2016**, *28*, 7203–7217.
- [18] J. Kang, F. Yan, P. Zhang, C. Du, *J. Power Sources* **2012**, *206*, 310–314.
- [19] S. M. Lee, S. H. Lee, J. S. Roh, *Crystals (Basel)* **2021**, *11*, 1–11.
- [20] J. I. Langford, A. J. C. Wilson, *J. Appl. Cryst.* **1978**, *11*, 102–113.
- [21] P. Lian, X. Zhu, S. Liang, Z. Li, W. Yang, H. Wang, *Electrochim. Acta* **2010**, *55*, 3909–3914.
- [22] R. Badam, M. Shibuya, B. S. Mantripragada, M. Ohira, L. Zhou, N. Matsumi, *Polym. J.* **2022**, *54*, 1355–1366.
- [23] M. Ayiania, M. Smith, A. J. R. Hensley, L. Scudiero, J. S. McEwen, M. Garcia-Perez, *Carbon N Y* **2020**, *162*, 528–544.
- [24] C. Ma, X. Shao, D. Cao, *J. Mater. Chem.* **2012**, *22*, 8911–8915.
- [25] Y. Tang, X. Wang, J. Chen, X. Wang, D. Wang, Z. Mao, *Energy Technol.* **2020**, *2000361*, 1–11.
- [26] S. G. Patnaik, R. Vedaranjan, N. Matsumi, *J. Mater. Chem. A Mater.* **2017**, *5*, 17909–17919.
- [27] Y. Kondo, T. Abe, Y. Yamada, *ACS Appl. Mater. Interfaces* **2022**, *14*, 22706–22718.
- [28] T. R. Jow, S. A. Delp, J. L. Allen, J.-P. Jones, M. C. Smart, *J. Electrochem. Soc.* **2018**, *165*, A361–A367.
- [29] E. Peled, S. Menkin, *J. Electrochem. Soc.* **2017**, *164*, A1703–A1719.
- [30] N. L. Hamidah, F. M. Wang, G. Nugroho, *Surf. Interface Anal.* **2019**, *51*, 345–352.
- [31] Y. Kondo, T. Abe, Y. Yamada, *ACS Appl. Mater. Interfaces* **2022**, *14*, 22706–22718.
- [32] W. Cai, C. Yan, Y.-X. Yao, L. Xu, R. Xu, L.-L. Jiang, J.-Q. Huang, Q. Zhang, *Small Structures* **2020**, *1*, 2000010.
- [33] T. Ramesh, R. Vedaranjan, N. Rajalakshmi, L. R. G. Reddy, *J. Mater. Sci. Mater. Electron.* **2020**, *31*, 1681–1690.
- [34] A. Habekost, *World J. Chem. Educ.* **2020**, *9*, 14–21.
- [35] J. Huang, H. Ge, Z. Li, J. Zhang, *Electrochim. Acta* **2015**, *176*, 311–320.
- [36] J. Huang, Z. Li, J. Zhang, *J. Power Sources* **2015**, *273*, 1098–1102.
- [37] T. Q. Nguyen, C. Breitkopf, *J. Electrochem. Soc.* **2018**, *165*, E826–E831.
- [38] T. P. Jayakumar, R. Badam, N. Matsumi, *ACS Appl. Energ. Mater.* **2020**, *3*, 3337–3346.
- [39] T. Kim, W. Choi, H. C. Shin, J. Y. Choi, J. M. Kim, M. S. Park, W. S. Yoon, *J. Electrochem. Sci. Technol.* **2020**, *11*, 14–25.
- [40] C. Choi, D. S. Ashby, D. M. Butts, R. H. DeBlock, Q. Wei, J. Lau, B. Dunn, *Nat. Rev. Mater.* **2020**, *5*, 5–19.
- [41] V. Augustyn, P. Simon, B. Dunn, *Energy Environ. Sci.* **2014**, *7*, 1597–1614.
- [42] A. Gomez-martin, J. Martinez-fernandez, M. Ruttert, M. Winter, T. Placke, J. Ramirez-rico, *Carbon N Y* **2020**, *164*, 261–271.
- [43] J. E. Harlow, S. L. Glazier, J. Li, J. R. Dahn, *J. Electrochem. Soc.* **2018**, *165*, A3595–A3601.
- [44] Y. Son, H. Cha, C. Jo, A. S. Groombridge, T. Lee, A. Boies, J. Cho, M. De Volder, *Mater Today Energy* **2021**, *21*, 100838.
- [45] B. Srimita Mantripragada, K. Sumala Patnaik, K. Higashimine, R. Badam, N. Matsumi, *Electrochim. Commun.* **2023**, *157*, 107616.
- [46] B. Srimita Mantripragada, R. Badam, N. Matsumi, *ACS Appl. Energ. Mater.* **2022**, *5*, 6903–6912.
- [47] J. Asenbauer, T. Eisenmann, M. Kuenzel, A. Kazzazi, Z. Chen, D. Bresser, *Sustain. Energy Fuels* **2020**, *4*, 5387–5416.
- [48] Q. Zhang, W. Cai, Y. X. Yao, G. L. Zhu, C. Yan, L. L. Jiang, C. He, J. Q. Huang, *Chem. Soc. Rev.* **2020**, *49*, 3806–3833.
- [49] E. Kazyak, K. H. Chen, Y. Chen, T. H. Cho, N. P. Dasgupta, *Adv. Energy Mater.* **2022**, *12*, DOI 10.1002/aenm.202102618.
- [50] Y. Liu, Y. Zhu, Y. Cui, *Nat. Energy* **2019**, *4*, 540–550.

Manuscript received: November 7, 2023

Revised manuscript received: December 19, 2023

Accepted manuscript online: January 3, 2024

Version of record online: February 8, 2024